Electromagnetic turbulence in increased-β plasmas in the Large Plasma Device

G. D. Rossi[1]†, T. A. Carter[1], B. Seo[3], J. Robertson[1], M. J. Pueschel[2], and P. W. Terry [4]

[1]University of California, Los Angeles, Los Angeles, California 90095, USA

[2]Dutch Institute for Fundamental Energy Research, Eindhoven, Netherlands

[3]Embry-Riddle Aeronautical University, Daytona Beach, Florida 32114, USA

[4]University of Wisconsin-Madison, Madison, Wisconsin 53706, USA

(Received xx; revised xx; accepted xx)

The variation of pressure-gradient driven turbulence with plasma β (up to $\beta \approx 15\%$) is investigated in linear, magnetized plasma. The magnitude of magnetic fluctuations is observed to increase substantially with increasing β. More importantly, parallel magnetic fluctuations are observed to dominate at higher β values, with $\delta B_\parallel/\delta B_\perp \approx 2$ and $\delta B/B_0 \approx 1\%$. Parallel magnetic fluctuations are strongly correlated with density fluctuations and the two are observed to be out of phase. The relative magnitude of and cross-phase between density and parallel magnetic field fluctuations are consistent with dynamic pressure balance ($P + \frac{B_0^2}{2\mu_0}$ = constant). A local slab model theory for electromagnetic, modified drift Alfvén waves, including parallel magnetic fluctuations, shows partial agreement with experimental observations.

1. Introduction

Turbulence driven by cross-magnetic-field pressure gradients arises in a variety of natural (e.g. the Earth's magnetosphere) and laboratory (e.g. magnetically confined plasmas for fusion energy application) settings. For magnetized plasmas where the ratio of thermal energy density to magnetic energy density, β is low, the pressure-gradient-driven instabilities and the resulting turbulence is expected to be largely electrostatic (Liewer 1985; Carreras 1997; Doyle 2007) as field-line bending or compression is energetically unfavorable. As β is increased, these instabilities are expected to become more electromagnetic and this change is associated with important qualitative and quantitative changes in turbulence dynamics. First, unstable drift waves couple to Alfvén waves, which can substantially modify linear mode properties and the nature of the resulting turbulence (Jenko & Scott 1999). Second, the nonlinear saturation mechanisms can be affected, modifying the turbulence amplitudes and wavenumber spectra (Pueschel & Jenko 2010; Pueschel et al. 2013; Whelan et al. 2018). Third, inherently electromagnetic structures of the turbulence like zonal fields or magnetic streamers can develop at a wide range of β values (Smolyakov et al. 2002). Fourth, the relative importance of electromagnetic transport processes with respect to electrostatic ones might increase with β as the electron heat flux along fluctuating magnetic field lines can carry a substantial part of the overall cross-field heat fluxes at high β (Rechester & Rosenbluth 1978; Weiland & Hirose 1992; Pueschel et al. 2008). Fifth, new instabilities can develop as electromagnetic terms that were previously ignored become significant; for example,

† Email address for correspondence: grossi@g.ucla.edu

in tokamaks a transition from electrostatic instabilities such as the ion temperature gradient (ITG) to electromagnetic instabilities like the kinetic ballooning mode (KBM) as β is increased (Candy 2005).

The study of turbulence and turbulent transport is critical to the development of viable magnetic confinement fusion devices. In order to maximize fusion power and access continuous operation via a large bootstrap fraction (Kikuchi 1993), fusion plasmas benefit from increased plasma β (Terry et al. 2015; Citrin et al. 2015). In finite β plasmas the role of magnetic fluctuations can become more important, changing the character of instabilities and the nature of the resulting anomalous transport (Rechester & Rosenbluth 1978; Candy 2005; Weiland & Hirose 1992). The mechanisms that lead to modified linear/nonlinear stability(Terry et al. 2021), changes in turbulent flow generation, and novel electromagnetic transport effects are still not fully understood (Lee et al. 2015; Snyder & Hammett 2001). Understanding pressure-gradient-driven turbulence in higher β plasmas is also of relevance to processes in near-Earth space including generation of coherent structures, energetic particle transport in the heliosphere and modification of magnetic reconnection in the presence of pressure gradients (Zimbardo et al. 2012; Pueschel et al. 2015).

This paper reports on experiments in which the variation of pressure-gradient-driven turbulence is documented as a function of plasma β. These experiments have been made possible through the use of a LaB_6 cathode plasma source in the Large Plasma Device (LAPD) (Gekelman et al. 2016). This source produces plasmas with up to a factor of 100 increase in plasma pressure compared to lower-power density plasma sources, which, along with lowered magnetic field, enable access to moderate β values ($\sim 0.1 - 1$) while maintaining ion magnetization. In these experiments, plasma β is varied from $\approx 0.2\%$ up to $\approx 15\%$. From the scan, normalized density fluctuations are seen to decrease slightly with increasing β while normalized magnetic fluctuations increase substantially, going from $\delta B/B_0 \sim 0.06\%$ at the lowest β to $\delta B/B_0 \sim 1\%$ at the highest β values. Importantly, parallel magnetic fluctuations represent a large fraction of the fluctuation amplitude; they are comparable in magnitude to perpendicular fluctuations at $\beta \sim 1\%$ but are a factor of two larger at the highest β. The magnitude of parallel magnetic fluctuations is consistent with dynamic pressure balance in the turbulence: $P + {B_0}^2/(2\mu_0) = \text{constant}$. The measurements are compared to predictions from a simple slab model of resistive drift-Alfvén waves, extended to include compressive magnetic fluctuations and increased β.

2. Experimental Setup

The Large Plasma Device (LAPD) (Gekelman et al. 2016), shown schematically in Fig. 2, produces an 18 m long cylindrical magnetized plasma using emissive cathode discharges. Two plasma sources are used during these experiments. The primary LAPD cathode is a 75cm BaO-coated nickel cathode that produces a 60cm diameter background plasma with density $n \sim 10^{12}$ cm^{-3}. A secondary plasma source has been installed on LAPD, utilizing a smaller LaB_6 cathode that can produce higher-power-density discharges leading to a higher density plasma column (≈ 20 cm diameter) Gekelman et al. (2016). The smaller LaB_6 cathode is installed on the opposite end of LAPD, allowing for simultaneous operation with the primary BaO cathode. For the experiments reported in this paper, a helium plasma with a density of 2×10^{13} cm^{-3} and peak electron temperature of $\sim$4 eV was produced by discharging the LaB_6 source in the afterglow of the primary BaO plasma source.

Previous experiments in LAPD have investigated turbulence driven by pressure-gradients and flow in the lower-β plasma produced by the BaO cathode. These studies have included: excitation of drift-Alfvén waves by filamentary structures (Morales et al. 1999; Peñano et al. 2000; Burke et al. 2000; Pace et al. 2008), intermittent turbulence and turbulent structures (Carter 2006; Pace et al. 2008; Maggs & Morales 2012), modification of turbulence and suppression of transport by sheared flow (Carter & Maggs 2009; Maggs et al. 2007; Zhou et al. 2012; Schaffner et al. 2013), flow and shear-flow driven instabilities (Horton et al. 2005, 2009; Schaffner et al. 2013) and avalanche transport events driven by pressure gradients (Van Compernolle & Morales 2017).

The experiments reported here build on this previous work, seeking to document changes to pressure-gradient-driven turbulence and associated transport as a function of plasma β. Increased plasma β is in part accessed through the higher pressure plasma produced by the LaB_6 source. Additional control over plasma β is accomplished through varying the background magnetic field. In this study, the field was varied from 1000G to 175G, resulting in a core plasma β range of 0.17% to 15% respectively. Diamagnetic modifications of the mean field are measured and at the highest β represent a 5% reduction in the applied background field. As the field strength is varied, Langmuir probe and line-averaged interferometer measurements confirm that the peak plasma density does not change substantially. Using the field strength to vary plasma β has its drawbacks as other dimensionless parameters are not held fixed in the scan; in particular $\rho^* = \rho_s/a$, where ρ_s is the ion sound gyroradius and a is scale length in the plasma, here taken to be the plasma diameter. This parameter varies from $\rho^* \sim 0.02$ to $\rho^* \sim 0.1$ over the range of magnetic field used in this study.

Measurements of the electron density, electron temperature, and potential (both plasma and floating potential) are made using Langmuir probes axially located in the center of the machine. Mean electron density profiles are determined using ion saturation current ($I_{\rm sat} \propto n\sqrt{T_e}$) measured by fixed-bias double Langmuir probe and electron temperature determined from triple Langmuir and swept Langmuir probes. The mean density profile measurements are calibrated using line-averaged density measurements made by a microwave interferometer. Mean plasma potential profiles are determined from high spatial resolution floating potential measurements which are calibrated to swept Langmuir probe measurements at specific radial locations. Plasma density and potential fluctuations are inferred from fluctuations in ion saturation current and in floating potential from a Langmuir probe; these signals are analyzed assuming that temperature fluctuations are negligible in order to infer characteristics of density and potential fluctuations. Measurements of magnetic field fluctuations are made with three-axis magnetic induction (or "B-dot") probes (Everson et al. 2009). Changes to the background magnetic field due to diamagnetic effects are determined using time-integrated measurements of $\dot{B}_z$ from the three-axis coils.

3. Experimental Results

Figure 2 shows profiles of the mean plasma density and electron temperature for different values of core beta (different values of applied magnetic field). The core plasma density and steepness of the edge gradient are similar for all beta values. Electron temperature grows significantly in width as lowering B_0 in the center of the machine while holding B_0 constant at the cathode sources to reach higher β causes flaring. A slight asymmetry in the profiles can be attributed to the perturbing nature of probe effects with a small target plasma. Diagnostics enter from the $r = 30$ cm side and must traverse the entire plasma column to measure the $r = -20$ cm side of the dataset. Thus,

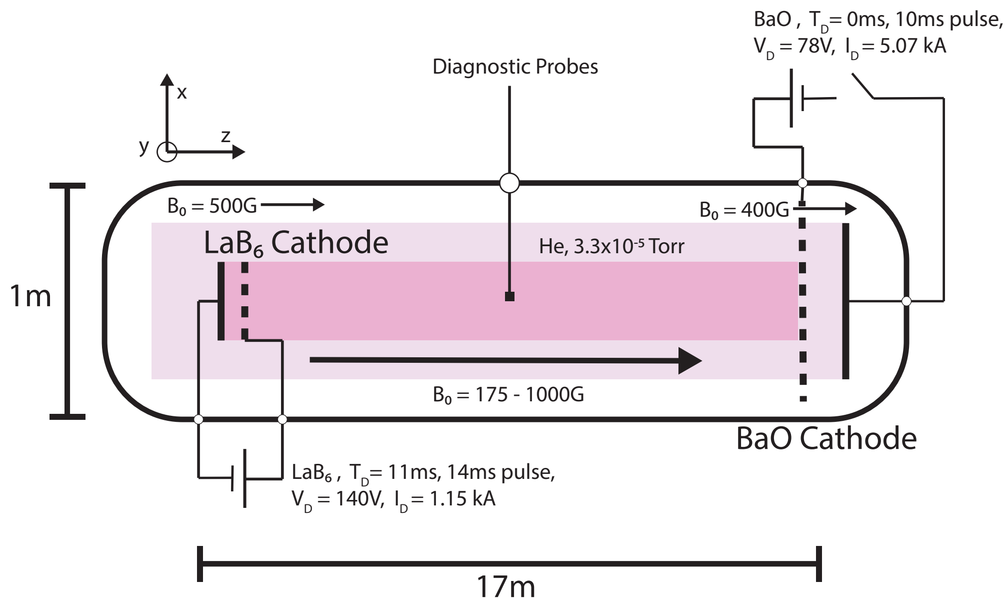

FIGURE 1. Schematic of the experimental setup on the LAPD (not to scale). Staggered discharges of both cathode sources and a reduction of the background field in the middle of the device are utilized to reach higher plasma β than during normal operation.

subsequent analysis in this paper will focus on the right side of the column where $r > 0$ cm.

A magnetic pick-up probe was used to measure the low-frequency variation of the background magnetic field due to diamagnetism; time traces of the the reduction of the magnetic field in the core plasma at four different β are shown in Fig. 3 with the reduction becoming more prominent with increasing β. By averaging the time traces from $t = 12$ to $t = 15ms$, radial profiles of the background magnetic fields, including their diamagnetic reductions, at different β can represented as the magnetic pressure ($P_{mag} = \frac{B_0^2}{2\mu_0}$) in Fig. 4. By also overlaying the plasma pressure ($P_{plasma} \approx n_e t_e$) and total pressure ($P_{plasma} + P_{mag}$) one can confirm that radial pressure balance:

$$P_{plasma} + \frac{B_0^2}{2\mu_0} = constant \tag{3.1}$$

is satisfied to within 2%.

The radial profiles of the mean plasma density along with temporal root-mean-square (RMS) density and magnetic field fluctuation amplitude for four different magnetic field values (four different core β values) are shown in Fig. 5. These four β conditions are chosen for Fig. 5 to highlight key changes in the turbulence as the relative amplitudes between $\delta B_{\|}, \delta B_{\perp}$, and δn_e change with β. Focusing first on the lowest β condition in Fig. 5a, peaks in density fluctuations are observed that are localized to the maximum density gradient regions. Focusing on the magnetic fluctuation profiles, it is observed that the perpendicular fluctuations are localized to the core. After lowering the field to increase β modestly to 1.1%, as seen in Fig. 5b), these perpendicular magnetic fluctuations begin to grow and the appearance of parallel magnetic fluctuations localized to the edge pressure gradients are first seen.

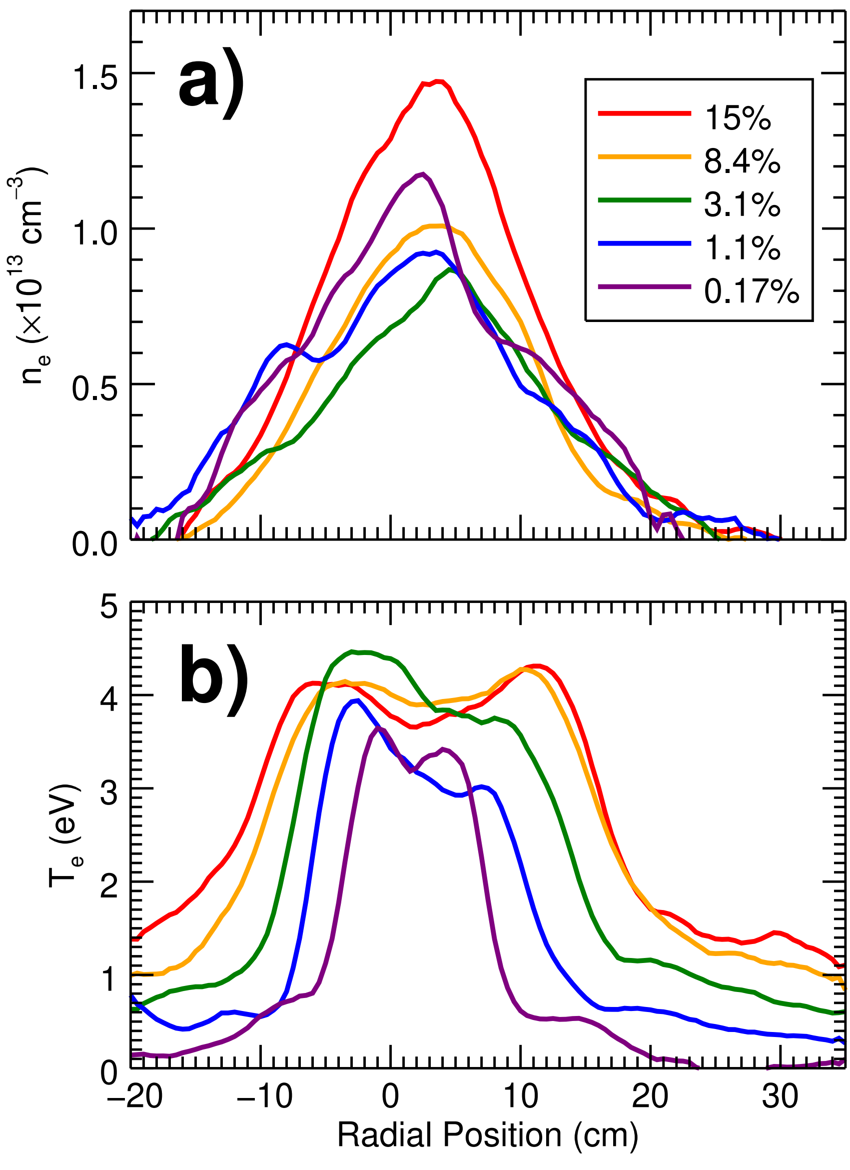

FIGURE 2. a) Density and b) electron temperature mean radial profile measurements for different values of core β. Core density is similar for all β whereas electron temperature grows significantly in width as the background field in the center of the machine is lowered to reach higher β.

The $\delta B_\parallel$ fluctuation spectra for $\beta = 1.1\%$, shown in Fig. 6, reveals that most of the power is concentrated at a low frequency peak ($\omega \sim .003\omega_{ci}$ where ω_{ci} is the ion cyclotron frequency) with additional semi-coherent peaks at higher frequencies. While not shown, the fluctuation spectra for δn_e and $\delta B_\perp$ are also very similar to that of $\delta B_\parallel$ and strongly correlated. This suggests that while the radial localization is different for some fluctuating quantities, these fluctuations are created by the same global mechanism.

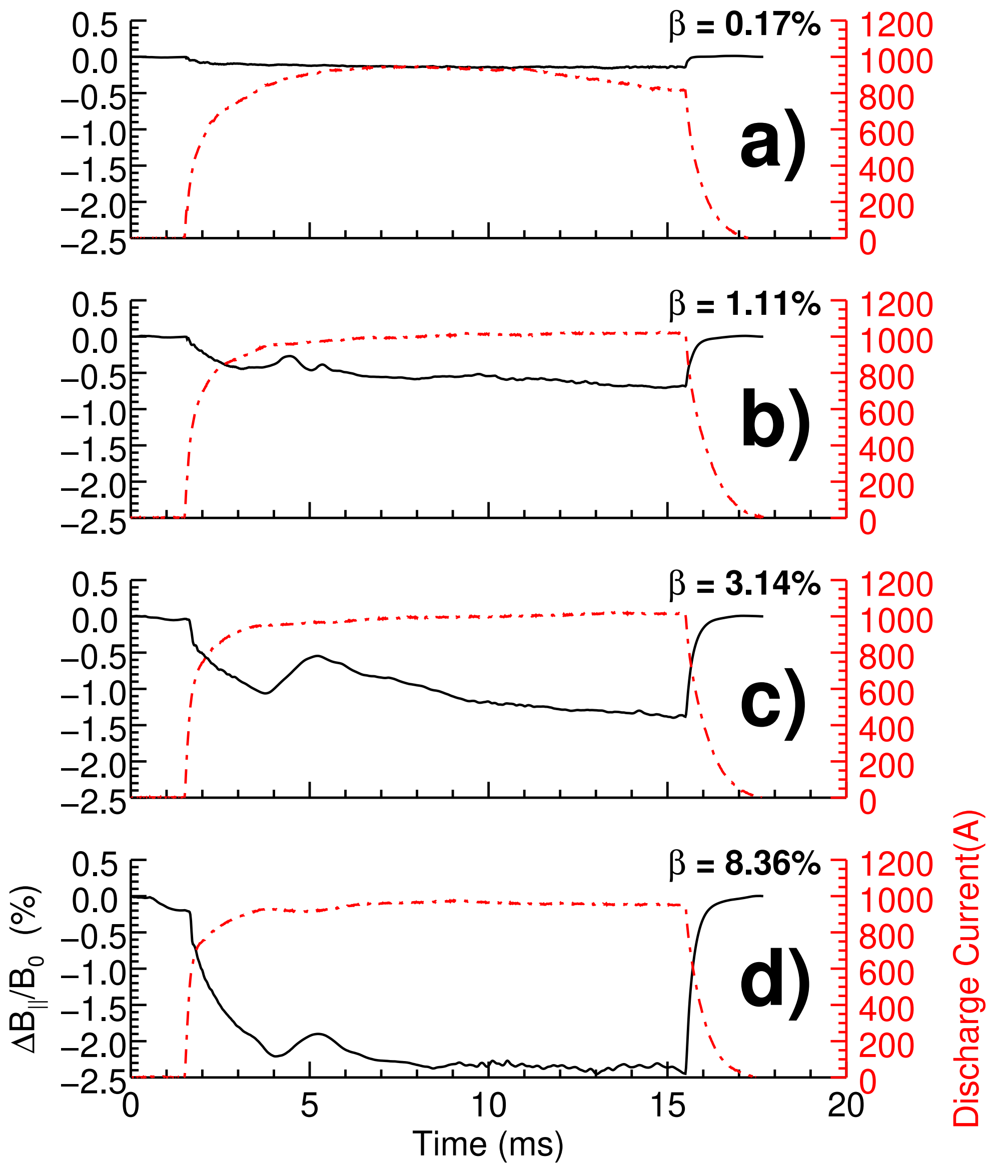

FIGURE 3. Time traces of normalized diamagnetic reductions to the background field (solid line) and discharge current to the LaB_6 cathode source (dashed line) at 4 different plasma β conditions, a) 0.17%, b) 1.1%, c) 3.1%, and d) 8.4%. Reduction increases with β

Core-localization of perpendicular magnetic fluctuations is consistent with previous observations of low-m drift-Alfvén waves in smaller plasma columns in LAPD (Burke et al. 2000). One can demonstrate that the observed fluctuations are low-m cylindrical eigenmodes by looking at the spectral 2D cross correlation C_{spec} between the different magnetic directions at the low frequency peaks seen in Fig. 6. This zero time-delay correlation function is computed in terms of an integral over the cross-spectrum between

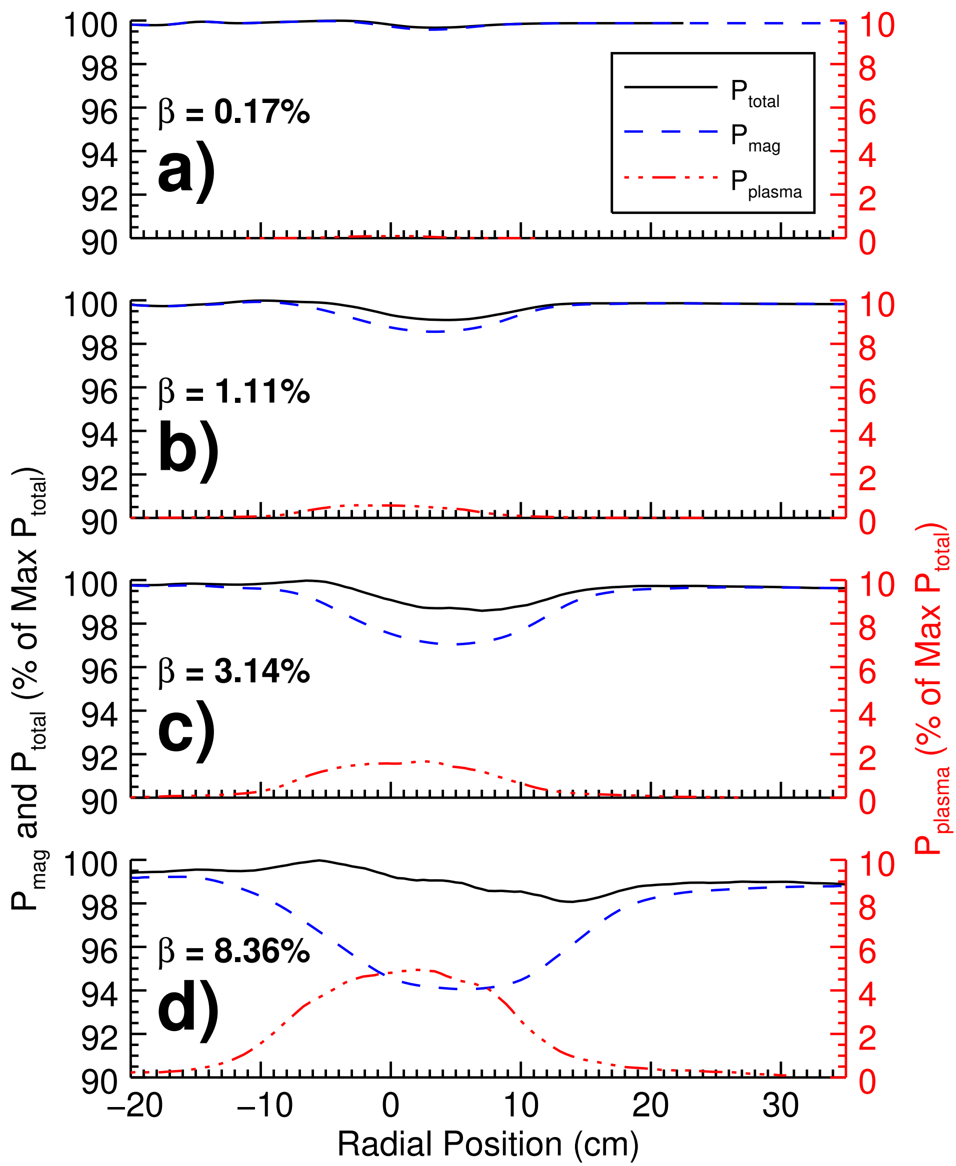

FIGURE 4. Radial profiles of magnetic and plasma pressure (dashed) as well as the sum (solid) normalized to the maximum total pressure at 4 different plasma β conditions, a) 0.17%, b) 1.1%, c) 3.1%, and d) 8.4%. Pressure balance holds (within 2%) as radial localization of increases in plasma pressure are matched with decreases in magnetic pressure.

the time series of a stationary reference probe (I_{ref}) and an axially offset moving probe (I_{mov}) for frequency bandwidths $[f-\delta, f+\delta]$. The function is as follows:

$$C_{spec}(x,y,\omega) = 2\int_{\omega-\delta}^{\omega+\delta} \|\tilde{I}_{ref}(x,y,\omega)\|\|\tilde{I}_{mov}(x,y,\omega)\|\cos(\theta)\gamma d\omega \qquad (3.2)$$

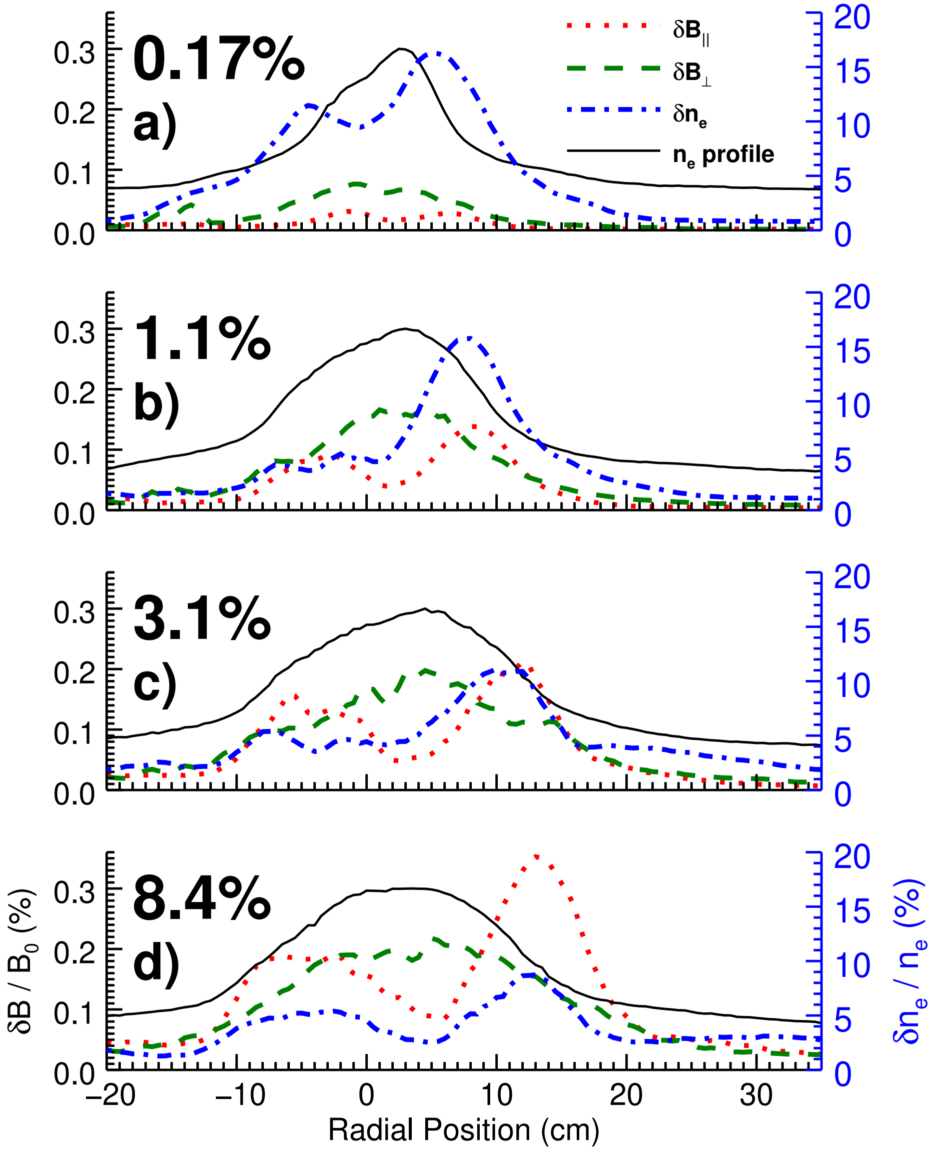

FIGURE 5. Mean density radial profile and density / magnetic temporal RMS fluctuation profiles at 4 different plasma β conditions,a) 0.17%, b) 1.1%, c) 3.1%, and d) 8.4%. $\delta B_{\parallel}$ and δn_e fluctuations are localized to the gradient region while $\delta B_{\perp}$ fluctuations are localized to the core for all β conditions.

whereby $C_{spec}(x, y, \omega)$ is normalized by C_{max} for the 2D plane, θ is the spectral crossphase between I_{ref} and I_{mov} fluctuations, and γ is the coherency between the two signals. Frequency bandwidths are small ($\delta = 0.0012\omega_{ci}$) and ω is chosen in order to isolate specific modes that display the clearest spatial structures.

Using this technique, for $\beta = 1.1\%$ it is observed in Fig. 7a that the $\delta B_{\parallel}$ structure is localized to the gradient edge region of the plasma, consistent with an $m = 1$ eigenmode

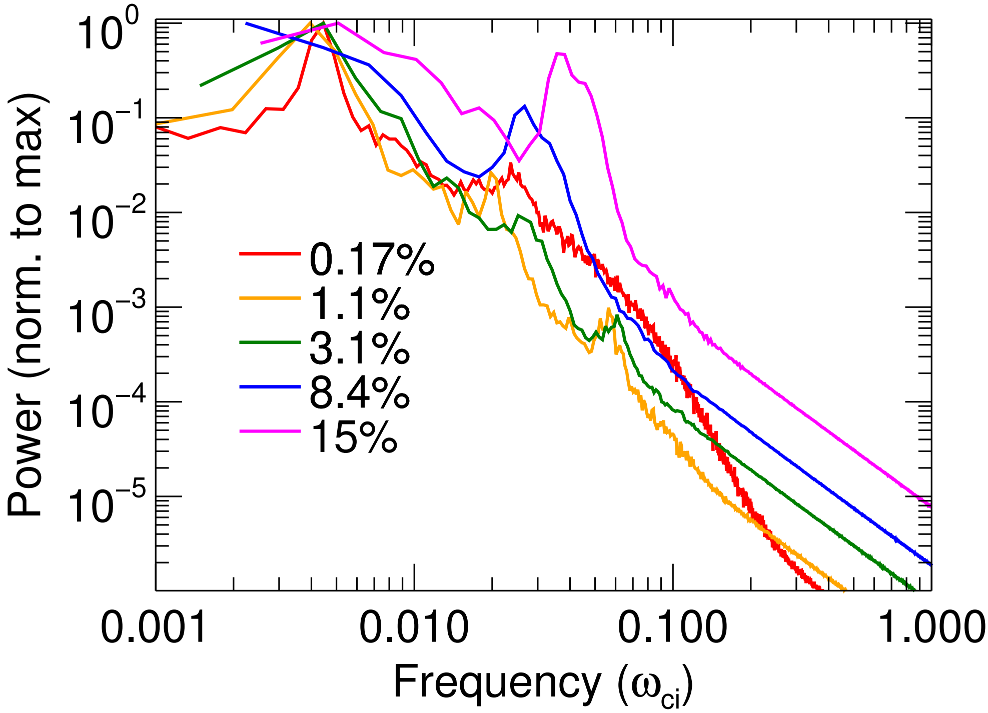

FIGURE 6. Power spectra of $\delta B_{\parallel}$ fluctuations for many β conditions. Most of the power is located at low frequency while peaks at higher frequencies grow in power with increasing β until the emergence a single coherent peak at the highest β.

and is coherent for higher frequency modes such as $m = 3$ seen in Fig. 7b. A slight discrepancy in the location of frequency peaks seen in Fig. 6 and the ω selected in Fig. 7 is due to the fact that the data collected to produce each figure are from different runs where slight changes in the plasma are expected.

Fig. 8a shows $B_{\perp}$ fluctuation power localized to the core of plasma while computing the parallel current $J_{\parallel}$ shows distinct current channels localized on the density gradient. These observations are consistent with a low-m drift-Alfvén wave, as will be shown in more detail below. Similar cross-correlation data was taken at higher values of β and seen to be qualitatively equivalent.

Continuing to increase β, as seen in Fig. 5c), the radial locations of the fluctuation peaks remain constant relative to the density profile. Focusing on the amplitude of the peaks, density fluctuations are seen to modestly decrease while both the parallel and perpendicular magnetic fluctuations increase with higher β. Of particular interest, at the highest β condition, as seen in Fig. 5d), the relative magnitude of $B_{\parallel}$ fluctuations exceeds that of $B_{\perp}$. This trend can be quantified by tracking the peak amplitude of the different types of fluctuations for additional intermediate plasma β conditions. As shown in Fig. 9a), this analysis demonstrates that both parallel and perpendicular fluctuations increase rapidly with increasing β until they diverge from one another at $\beta \sim 2\%$. For $\beta > 2\%$ peak parallel fluctuation level continues to increase, albeit at a slower rate, while perpendicular fluctuations saturate and remain mostly constant until reaching the

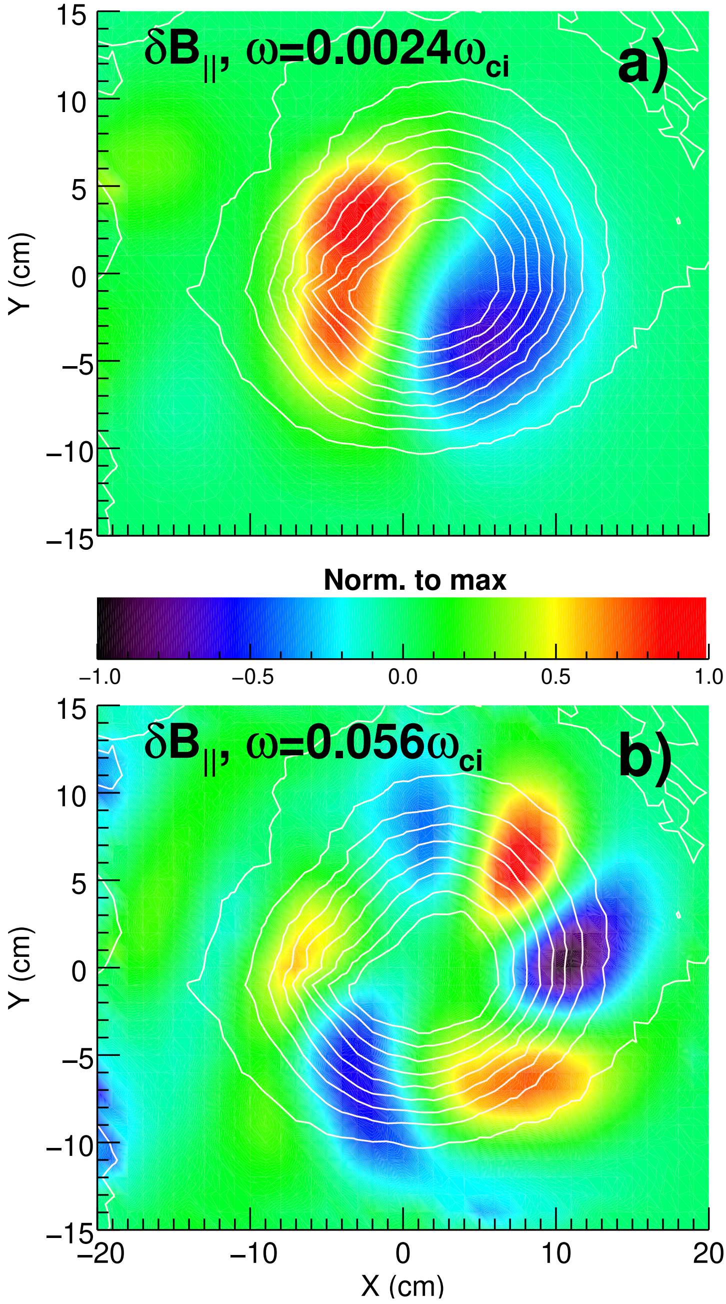

FIGURE 7. a) Cross-spectral power between a moving $B_\parallel$ and stationary n_e probe at $\beta = 1.1\%$ for a) $\omega \approx 0.0024\omega_{ci}$ showing a coherent m = 1 structure and b) $\omega \approx 0.056\omega_c i$ showing an m = 3 structure. The contour lines map out the density profile.

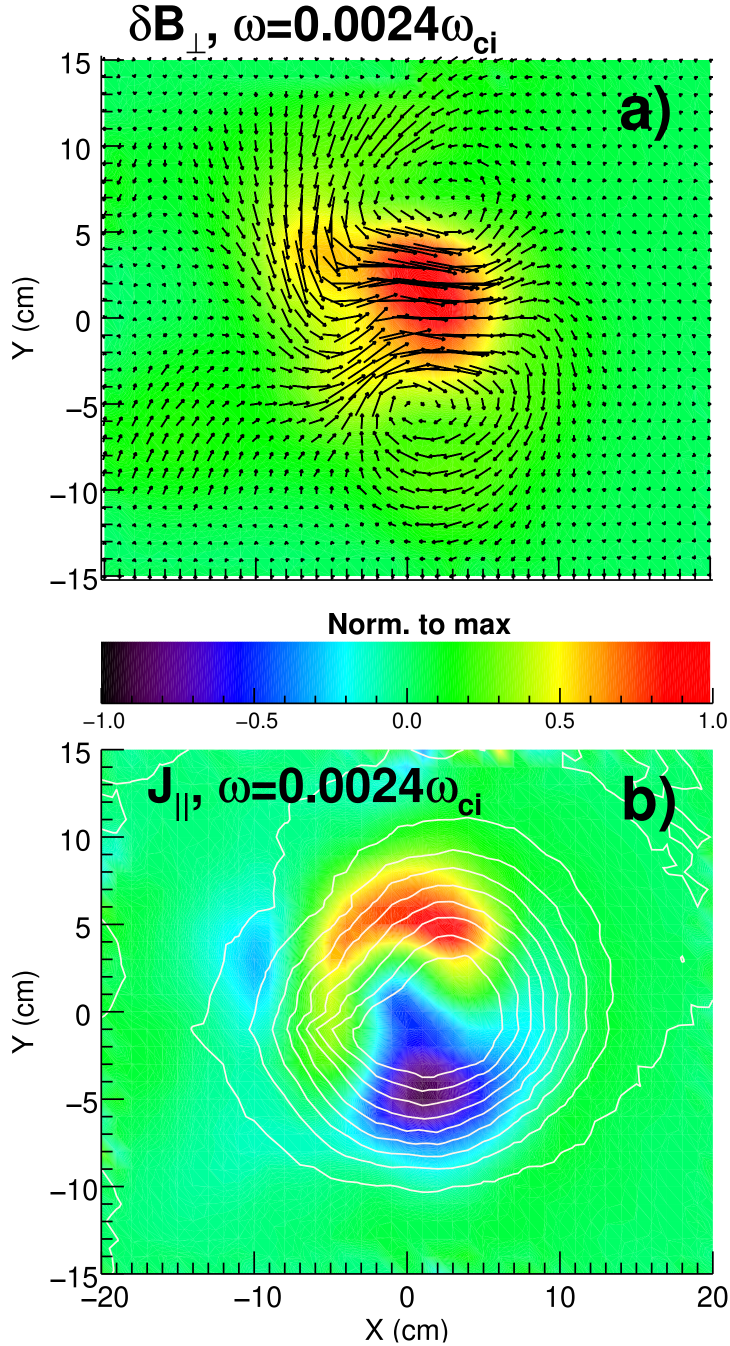

FIGURE 8. a) Cross-spectral power between a moving $B_\perp$ and stationary n_e probe at $\beta = 1.1\%$ for $\omega \approx 0.0024\omega_{ci}$ with B_x, B_y vectors on top. Pattern matches the expected core localization for a drift-Alfvén wave. b) Parallel current calculated from $\nabla \times \mathbf{B}_\perp$ that matches the expected current channels on the density gradient. The contour lines map out the density profile.

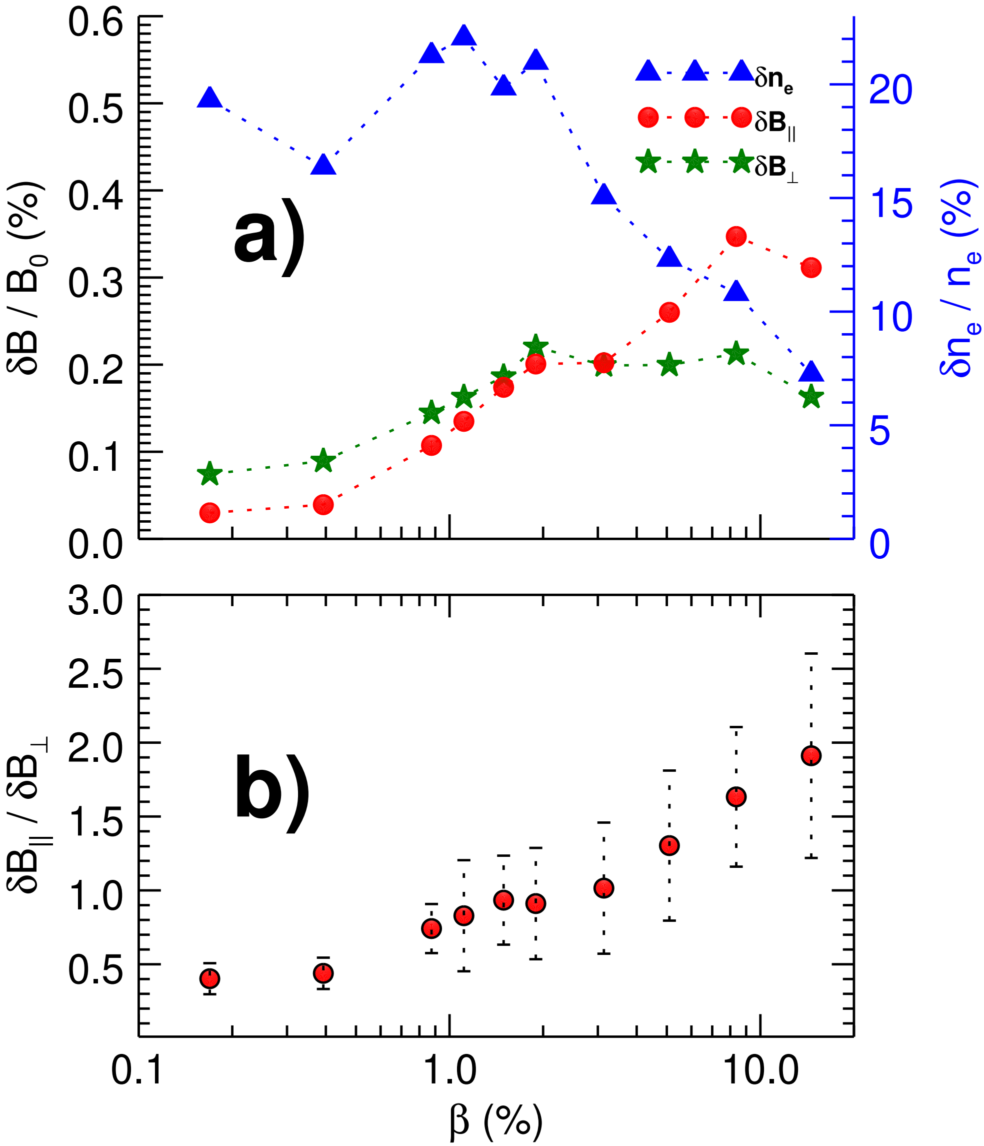

FIGURE 9. a) Peak RMS fluctuation levels for magnetics and density as a function of plasma β. Here $\delta B_{\parallel}$,$\delta B_{\perp}$ grow with β while δn_e decreases. b) Ratio of parallel to perpendicular magnetic peak RMS fluctuation power which also increases past order unity for $\beta \geqslant 2\%$.

highest $\beta > 10\%$ conditions of the data set.Figure 9(b) quantifies this trend by analyzing the ratio of parallel to perpendicular magnetic RMS (temporal) fluctuation levels. This ratio is shown to grow beyond order unity for $\beta \geqslant 2\%$ and reach a factor of 2 at the highest β.

Characterizing this unique growth of $B_{\parallel}$ fluctuations, changes in fluctuation spectra at different β conditions are analyzed. Fig. 6 shows how low frequency fluctuations are dominant for all β conditions. At the lower β there are multiple higher frequency peaks which correspond to the higher m-number mode structures such as the m = 3 seen in Fig. 7b.As β increases, these multiple higher frequency peaks disappear and a single coherent peak at $\approx .02\ \omega_{ci}$ arises.

One physical mechanism for generation of parallel magnetic field perturbations is perturbed diamagnetic currents that arise due to density fluctuations in an increased β plasma. This mechanism is equivalent to dynamic pressure balance between the magnetic and plasma pressure fluctuations. From Eq. 3.1, pressure balance can be written for the fluctuation quantities as

$$\frac{\delta P}{B_0^2/\mu_0} = -\frac{\delta B_{\|}}{B_0} \tag{3.3}$$

such that

$$\frac{\delta(n_e T_e)}{B_0^2/\mu_0} = -\frac{\delta B_{\|}}{B_0}. \tag{3.4}$$

From Eq. 3.3 it is predicted that $B_{\|}$ and δP fluctuations should be out of phase by π radians with one another and that the left and right side should be on the same order of magnitude. Fig. 10 confirms this with $\delta P/(B_0^2/\mu_0)$ and $\delta B_{\|}/B_0$ having the correct sign and having a fairly good linear fit to the predicted 1:1 relationship.

The prediction in Eq. 3.4 can be further validated by looking at cross-correlation functions between $\delta B_{\|}$ and δn_e fluctuations. Fig. 11a) shows the same spectral band passed cross-correlation function, C_{spec}, from Fig. 7 between two n_e probes located 5 meters apart in the axial direction at $\beta = 1.1\%$. One probe is stationary on the density gradient at $r = 10$ cm while the other traverses the plasma column in the XY plane and the signals are correlated to one another using the same technique as Eq. 3.2.

The area outlined by the black dotted line indicates the location of the stationary probe $(x_{\text{ref}}, y_{\text{ref}})$ as it is the location of highest correlation. Fig. 11b) uses the same stationary probe as Fig. 11a) but is instead correlated to a moving $B_{\|}$ probe located 5.5m away axially. As seen from the outlined circle, which represents the position of the stationary n_e probe, the fluctuations between $B_{\|}$ and n_e appear to be highly anti-correlated. This is consistent with the theory of pressure balance.

One can now compute $C_{spec}(x_{\text{ref}}, y_{\text{ref}}, \omega)$ at the location of the stationary n_e probe for a larger frequency range. Doing so allows for the individual contributions such as the coherence γ and phase difference θ between $B_{\|}$ and n_e fluctuations at all frequencies to be quantified. As seen in Fig. 12a), there are a few semi-coherent peaks on top of a broadband spectrum which are primarily due to the corresponding peaks in cross-coherence between the two signals as seen in Fig. 12b). From Fig. 12c) it is observed that for all low frequencies the cross-phase between n_e and $B_{\|}$ is π radians out of phase.

Investigating further, a decomposition of the polarization of the wave to be either right-handed (rotating in the electron direction) or left-handed (ion direction) can be made. This technique involves summing together Fourier transforms of B_x and B_y core fluctuations in frequency space and adding phase differences of $+\frac{\pi}{2}$ (right-handed) or $-\frac{\pi}{2}$ (left-handed) (Weidl et al. 2016; Terasawa et al. 1986) as follows:

$$\begin{aligned} \widetilde{B_L}(\omega) &= \frac{1}{2}[\widetilde{B_x}(\omega) + i\widetilde{B_y}(\omega)] \\ \widetilde{B_R}(\omega) &= \frac{1}{2}[\widetilde{B_x}(\omega) - i\widetilde{B_y}(\omega)] \end{aligned} \tag{3.5}$$

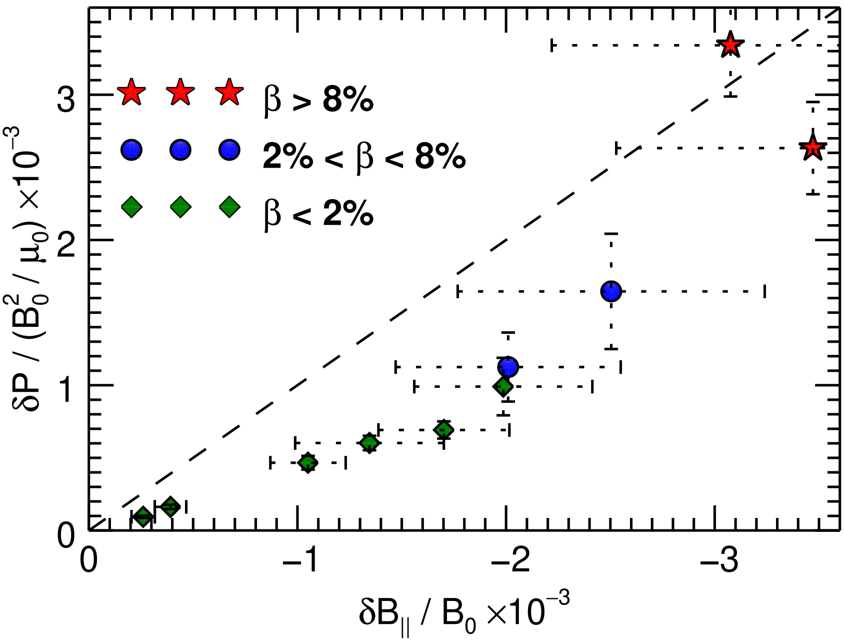

FIGURE 10. Pressure balance, $\delta P({B_0}^2/\mu_0)$ vs. $\delta B_{\parallel}/B_0$ for different β conditions. Dotted line represents the expected result for pressure balance which is qualitatively consistent and follows the correct trend for different β.

where $\widetilde{B_x}(\omega)$ is the Fourier transform of B_x. $\widetilde{B_{L,R}}(\omega)$ are then transformed back to the time domain and by analyzing the power of the RMS fluctuations in each case one can determine whether the instability is primarily right or left-handed by defining percent power as

$$\%\,Left = \frac{\|\delta B_L\|^2}{\|\delta B_L\|^2 + \|\delta B_R\|^2}. \tag{3.6}$$

Repeating this analysis for many β conditions, as seen in Fig. 13 it is concluded that the wave is predominantly left-handed for low β conditions. However, as β increases, there is a distinct shift where the turbulence changes to become more right-handed in nature. Since drift-Alfvén waves are typically left-hand polarized, this analysis further points to the turbulence being caused by a modified drift-Alfvén for the majority of β conditions studied in this experiment. The deviation to right-hand polarization at the higher β conditions could indicate a new instability developing and explain the multiple higher frequency peaks coalescing around a single peak for $\beta > 10\%$ as seen in Fig. 6.

4. Discussion

Initial observations led to a proposal that the data could be the result of a new instability, the Gradient-driven Drift Coupling mode or GDC instability (Pueschel et al. 2011, 2015, 2017). The GDC was originally observed in kinetic simulations of magnetic reconnection and had characteristics similar to those observed in the LAPD data, in particular correlated density and parallel magnetic field fluctuations with the magnetic field fluctuations out of phase with the density fluctuations. Kinetic

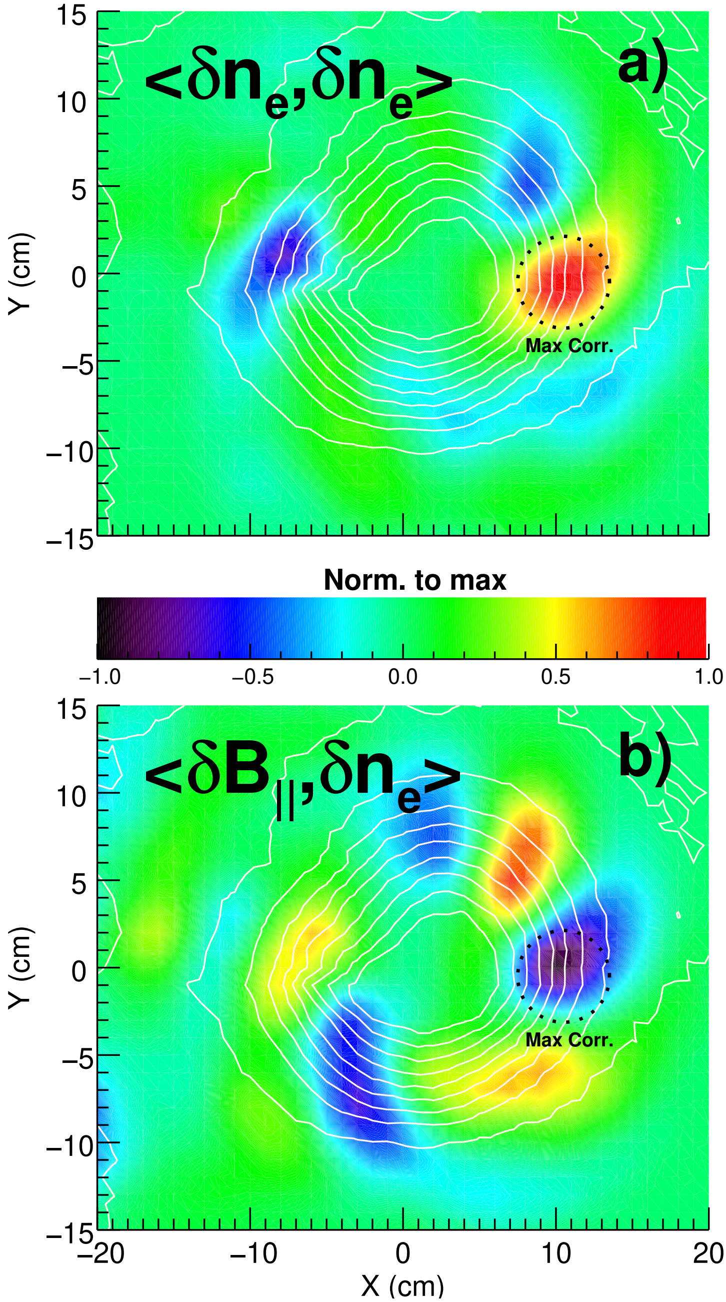

FIGURE 11. Strong anti-correlation at $\beta = 1.1\%$ of δn_e and $\delta B_\parallel$ fluctuations by showing a) cross correlation between a moving n_e and stationary n_e probe with b) correlation between a moving $B_\parallel$ and the same stationary n_e probe with the dotted circle indicating the location of maximum correlation from a). The contour lines map out the density profile.

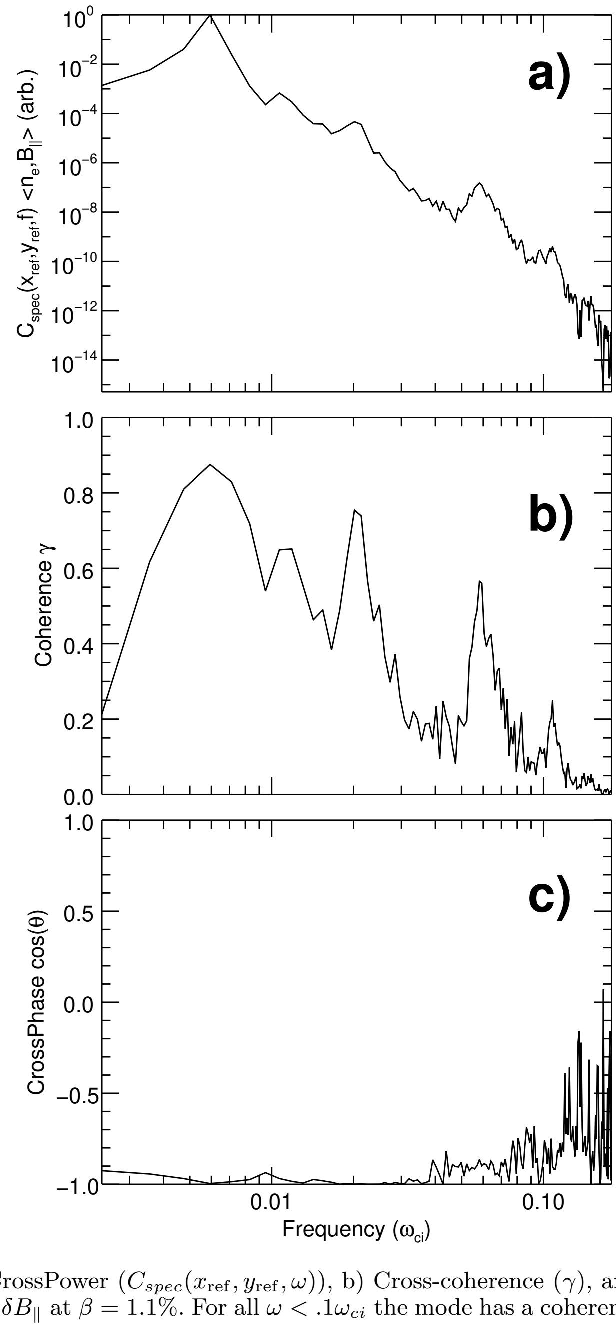

FIGURE 12. a) CrossPower ($C_{spec}(x_{\rm ref}, y_{\rm ref}, \omega)$), b) Cross-coherence ($\gamma$), and c) cross-phase ($\theta$) between δn_e and $\delta B_{\|}$ at $\beta = 1.1\%$. For all $\omega < .1\omega_{ci}$ the mode has a coherent $\frac{\pi}{2}$ phase difference.

simulations with LAPD pressure profiles and parameters indicated growth of the GDC in plasmas relevant to these experiments (Whelan et al. 2018). However, it was pointed out that the simulations that gave rise to the GDC as a new instability were run in out-of-equilibrium conditions, with pressure gradients but not including the gradients in the background magnetic field that should arise in pressure balance in finite β plasmas and are observed in this dataset. Exact force balance causes the GDC to become linearly marginally stable (Rogers et al. 2018). In addition, the GDC simulations do not predict

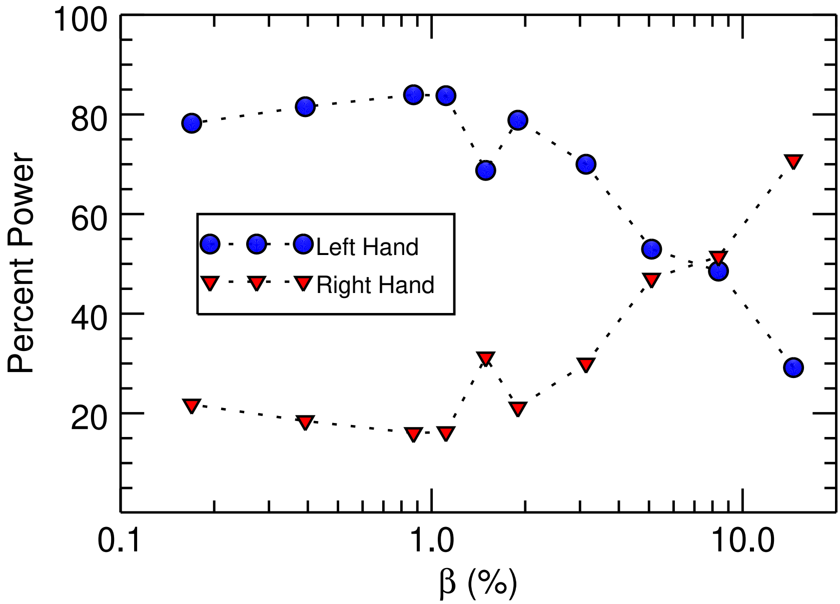

FIGURE 13. Power-weighted handedness of $\delta B_\perp$ fluctuations at various β conditions. Instability changes from left-handed to right-handed dominant with increasing β.

correlated perpendicular magnetic fluctuations as observed in the experimental data. Recent simulations of the GDC in electron-positron plasmas indicate that the GDC can nonlinearly persist in plasmas where radial pressure balance exists (where gradients in the background field develop) (Pueschel et al. 2020) and as such we do not rule out the possibility that the GDC could play a role in the saturated turbulent state that is observed in the experiments.

Nonetheless, given the similarity of the observed fluctuations in low β conditions to drift-Alfvén waves, it would be remiss to not pursue whether the observed modes are modified drift-Alfvén waves. At lower β, the characteristics of the observed fluctuations are consistent with previous observations of low-m drift-Alfvén waves in LAPD. In particular, the mode pattern of correlated perpendicular magnetic and density fluctuations and the polarization of the perpendicular magnetic fluctuations are fully consistent. As β is increased, parallel magnetic fluctuations grow, correlated with the perpendicular magnetic and density fluctuations. This observation is not consistent with the standard picture of the drift-Alfvén wave and motivates the following investigation of a modified drift-Alfvén wave theory.

A local, slab-model linear theory has been developed, starting from a Hall-MHD derivation of drift-Alfvén waves outlined by Goldston (Goldston & Rutherford 1995). Additional terms were added to include fluctuations in the background magnetic field and including non-uniform background field that arises due to diamagnetic effects at increased plasma β. The ordering of additional terms was determined by using experimental

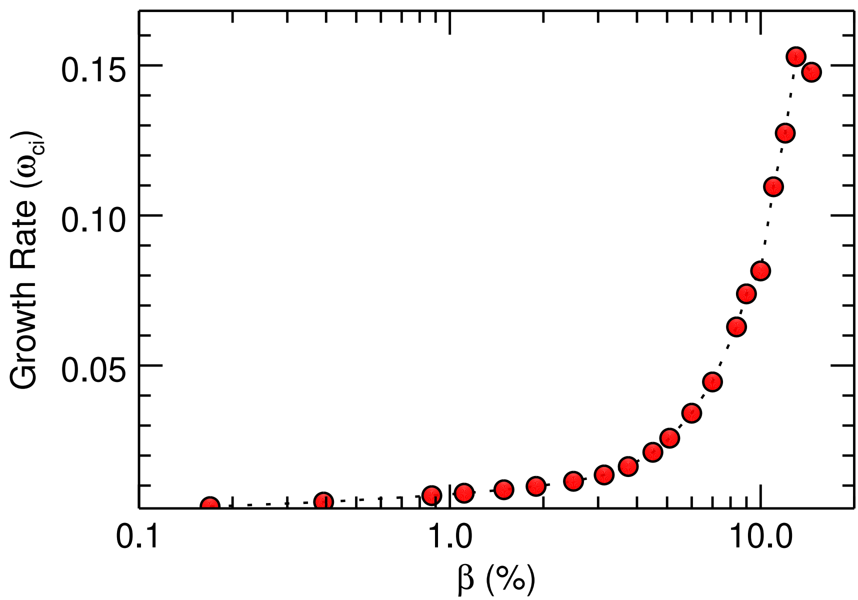

FIGURE 14. Growth rate of fastest growing mode from local theory at various β conditions.

measurements of the amplitude of fluctuating quantities. The resulting linear model is detailed in Appendix A.

Growth rates and instability characteristics of this model are computed using experimentally measured profiles for the lowest β condition and assuming $\lambda_{\parallel} = 2L_{\parallel}$ (where $L_{\parallel}$ is the axial length of the machine). By then decreasing B_0, one can perform a scan in plasma β. As shown in Fig. 14, for all values of β there appears to be an unstable mode and the growth rate increases with β.

In addition, this local theory can be used to compute ratios of amplitudes and phase differences for various fluctuating quantities in order to compare to experimental results. As detailed in Appendix A, the amplitude ratio between $\delta B_{\parallel}$ and δn can be be derived as follows:

$$\frac{\delta B_z/B_0}{\delta n_e/n_e} = \frac{\beta}{2} \times \frac{-k_x^2 - \partial_x \log(B_0)\partial_x \log(T_e) - ik_x\partial_x \log(B_0) + ik_x \partial_x \log(T_e)}{k_x^2 + (\partial_x \log(B_0))^2} \tag{4.1}$$

Figure 15 shows this ratio computed, using experimentally measured profiles and the ω and $k_{\perp}$ of the fastest growing mode for each β, along with experimental measurements. There is relatively good agreement between the linear theory prediction and experimental measurement for $\beta < 2\%$ with deviations at the higher β. The ratio between $\delta B_{\parallel}$ and $\delta B_{\perp}$ can also be computed from the model (see Appendix A:

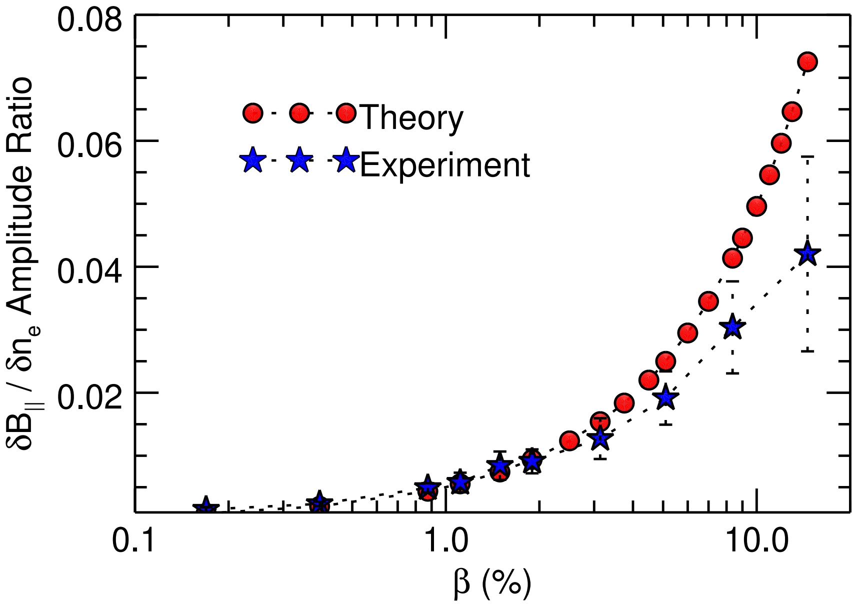

FIGURE 15. Ratio of parallel magnetic to density fluctuation amplitude as a function of β.

$$\frac{\delta B_\parallel}{\delta B_x} = \frac{\left(\begin{gathered} \frac{ik_\parallel}{\mu_0}B_0 - \frac{i}{k_\parallel B_0}\partial_x T_e \partial_x n_e + \frac{k_x}{k_\parallel B_0} n_e \partial_x T_e \\ - \frac{\omega^2}{k_\parallel B_0(\omega^2 - c_s^2 k_\parallel^2)} \partial_x n_e \left(k_x T_e + i\partial_x T_e\right) \\ + \frac{\omega}{(\omega^2-c_s^2k_\parallel^2)}\partial_x n_e \left(k_xT_e + i\partial_x T_e\right)\left(\frac{\frac{k_\parallel}{\omega B_0} v_A^2 (k_\perp^2 - i\frac{k_x}{B_0}\partial_x B_0)}{k_\perp^2 - \frac{1}{B_0^2} ik_x\partial_x B_0 - \frac{1}{B_0^2}\partial_x^2 B_0 + \frac{1}{B_0^3}(\partial_x B_0)^2}\right) \\ + \frac{\omega k_\parallel}{(\omega^2-c_s^2k_\parallel^2)}\frac{k_xT_e}{\omega m\mu_0}\partial_x B_0 + \frac{k_xT_e}{k_\parallel B_0}\partial_x n_e - i\frac{\omega k_\parallel}{(\omega^2-c_s^2k_\parallel^2)\omega m \mu_0}\partial_x T_e\partial_x B_0 \\ - i\frac{\partial_x T_e}{k_\parallel B_0}\partial_x n_e - i\omega\rho_0 \left(\frac{\frac{k_\parallel}{\omega B_0} v_A^2 (k_\perp^2 - i\frac{k_x}{B_0}\partial_x B_0)}{k_\perp^2 - \frac{1}{B_0^2} ik_x\partial_x B_0 - \frac{1}{B_0^2}\partial_x^2 B_0 + \frac{1}{B_0^3}(\partial_x B_0)^2}\right) \end{gathered}\right)}{\left(\begin{gathered} \frac{ik_x}{\mu_0}B_0 + \frac{1}{\mu_0}\partial_x B_0 \\ + \frac{\omega}{(\omega^2-c_s^2k_\parallel^2)}\partial_x n_e \frac{(k_xT_e+i\partial_xT_e)}{\left(k_\perp^2 - \frac{1}{B_0^2} ik_x\partial_x B_0 - \frac{1}{B_0^2}\partial_x^2 B_0 + \frac{1}{B_0^3}(\partial_x B_0)^2\right)}\left(\frac{\omega k_x}{B_0} + \frac{i\omega}{B_0^2}\partial_x B_0\right) \\ - i\omega^2\rho_0 \left(\frac{\left(\frac{k_x}{B_0}\right) + \frac{i}{B_0^2}\partial_x B_0}{k_\perp^2 - \frac{1}{B_0^2} ik_x\partial_x B_0 - \frac{1}{B_0^2}\partial_x^2 B_0 + \frac{1}{B_0^3}(\partial_x B_0)^2}\right) \end{gathered}\right)} \tag{4.2}$$

By performing a comparison of the theoretical predictions to experimental results as seen in Fig. 16, the ratio of these fluctuations increase with β in a similar fashion to the experimental results for $\beta < 2\%$. While the parallel wavelength of the mode was not able to be measured directly, the theoretical predictions suggest that $\lambda_{||}$ is many machine lengths as seen with the improved agreement for larger $\lambda_{||}$.

While the experimental data is consistent with the predictions of the slab-based local

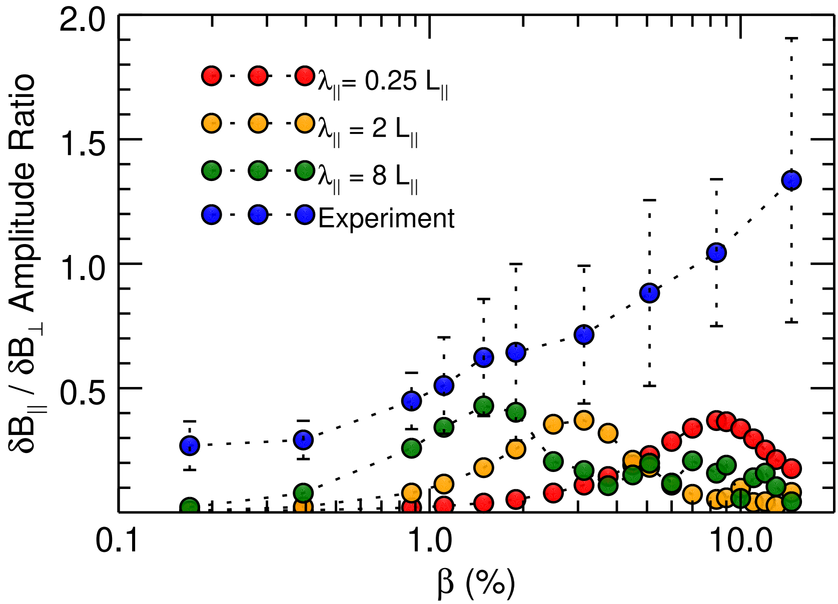

FIGURE 16. Ratio of parallel to perpendicular magnetic fluctuation amplitude for experimental data and using a theoretical model with different values of $\lambda_{\parallel}$ where $L_{\parallel}$ is the axial length of the machine. Ratio is seen to generally increase with increasing β with the best agreement between theory and experiment at higher $\lambda_{\parallel}$.

model at lower β, that agreement begins to break down at higher $\beta > 2\%$. This could be explained by finite Larmor radius (FLR) effects becoming important as lowering the background magnetic field to increase β also increases the ion gyroradius such that only a few ion gyroradii fit within the pressure gradients of the experiment. Future work will seek to address this through the development of a global kinetic model that includes significant $\delta B_{\parallel}$ fluctuations in order to capture more of the physics involved with the predominantly low-m modes observed.

5. Conclusions

In this experiment, the variation of pressure-gradient-driven turbulence and transport for increased β (up to $\beta \approx 15\%$) is documented in a linear, magnetized plasma. Magnetic fluctuations are observed to grow with increasing beta. A novel result is that parallel magnetic fluctuations are dominant at higher β, increasing up to $\delta B_{\parallel}/\delta B_{\perp} \approx 2$ with $\delta B/B_0 \approx 1\%$. Parallel magnetic fluctuations are also strongly correlated with density fluctuations, which are observed to be out of phase with one another. Further analysis of fluctuation amplitude ratios between δn_e and $\delta B_{\parallel}$ shows consistency with dynamic pressure balance ($P + \frac{B_0^2}{2\mu_0} =$ constant). Consistency of the measured mode pattern with previous observations of drift-Alfvén waves motivates the derivation of a local slab-model theory for electromagnetic, modified drift Alfvén waves that includes parallel magnetic fluctuations and diamagnetic corrections to the background field. Comparison of turbulence characteristics between this theoretical model and experimental data shows promising agreement for $\beta < 2\%$ while differences at higher β prompts the need for future work in developing a global kinetic model to illuminate whether the differences are the result of a new instability or further modifications to a drift-Alfvén wave.

6. Acknowledgements

The authors thank Z. Lucky, M. Drandell and P. Pribyl for technical support in executing the experiments.

7. Funding

This work was performed using the Basic Plasma Science Facility, which is supported by US DOE and NSF. Support for this work came from DOE awards DE-FC02-07ER54918:0023, DE-SC0014113:0003; and from NSF award PHY-1561912:004.

8. Declaration of interest

The authors report no conflict of interest.

Appendix A

In order to derive a dispersion relation for electromagnetically modified drift waves, we follow Goldston's (Goldston & Rutherford 1995) analysis but to carry through terms involving $\delta B_{\parallel}$ fluctuations and diamagnetic responses to the background field $\partial_x B_0$ that would normally be neglected.

This derivation assumes slab model plasma with a non-uniform density $n(x)$ whereby equilibrium is maintained by a strong background magnetic field, B_0. The plasma is also assumed to be at rest in the lab frame ($\mathbf{u} = 0$) but with a non-zero current density $J_y(x)$ which provides the $\mathbf{J} \times \mathbf{B}$ force to balance ∇P.

Starting with the perturbed equation of motion:

$$\begin{aligned} \rho_0 \partial_t \delta \mathbf{u} &= -\nabla \delta P + \delta(\mathbf{J} \times \mathbf{B}) \\ &= -\nabla \left(\delta P + \frac{\mathbf{B_0} \cdot \delta \mathbf{B}}{\mu_0} \right) + \frac{1}{\mu_0} \delta \left[(\mathbf{B} \cdot \nabla) \mathbf{B} \right]. \end{aligned} \tag{A 1}$$

one use Ohm's law to expand the $\hat{x}$ component to become

$$\begin{aligned} k_\perp^2 \delta u_x = \frac{1}{B_0^2} \partial_x \delta u_x \partial_x B_0 + \frac{1}{B_0^2} \delta u_x \partial_x^2 B_\parallel - \frac{\delta u_x}{B_0^3} \left(\partial_x B_0 \right)^2 \\ - \frac{k_\parallel \delta B_x}{\omega B_0} v_A^2 \left(k_\perp^2 - \frac{k_x}{B_0} \partial_x B_0 \right) + \omega k_x \frac{\delta B_\parallel}{B_0} + i\omega \frac{\delta B_\parallel}{B_0^2} \partial_x B_0 \end{aligned} \tag{A 2}$$

where $v_A^2 = \frac{B_0^2}{\mu_0 \rho_0}$ is the Alfvén speed and $k_\perp^2 = k_x^2 + k_y^2$. In order to now link δu_x, δB_x, and $\delta B_\parallel$, one can combine Faraday's law ($\partial_t \delta B_\parallel = -\nabla \times \delta \mathbf{E}$) and Ampere's law ($\nabla \times \mathbf{B} = \mu_0 \mathbf{J}$) with Ohm's law for first-order perturbed quantities ($\delta \mathbf{E} + \delta \mathbf{u} \times \mathbf{B} = \eta \delta \mathbf{J} + \frac{\mathbf{1}}{ne} \delta [\mathbf{J} \times \mathbf{B} - \nabla P_e]$ where η is resistivity) to obtain

$$\omega\delta B_x + k_\parallel B_0\delta u_x = -\frac{i\eta}{\mu_0}\delta B_x k_\perp^2 - \frac{k_y}{ne}\left(ik_\parallel\delta P_e + \frac{\delta B_x}{B_0}\partial_x P_e\right) \tag{A 3}$$

where it is assumed $\omega \ll \omega_{ci}$. If one also assumes that T_e is uniform along the field lines ($\mathbf{B}\cdot\nabla T_e = 0$) but can have a gradient across the field, one can use this in conjunction with the continuity equation ($\partial_t n + \nabla\cdot n\mathbf{u} = 0$) to rewrite the $\hat{z}$ component of Eq. A 1 as

$$ik_\parallel\delta n_e + \frac{\delta B_x}{B_0}\partial_x n_e = \frac{\omega}{B_0}\partial_x n_e\left(\frac{\omega\delta B_x + k_\parallel\delta u_x B_0}{\omega^2 - c_s^2k_\parallel^2}\right) + \frac{-k_\parallel^2\delta B_x\partial_x B_0}{m\mu_0(\omega^2 - c_s^2k_\parallel^2)} \tag{A 4}$$

where $c_s = \sqrt{\frac{T_e}{M}}$ is the plasma sound speed. Now substituting Eq. A 4 into Eq. A 3 results in

$$(\omega\delta B_x + k_\parallel B_0\delta u_x)\left(1 - \frac{k_y\omega v_{de}}{\omega^2 - c_s^2k_\parallel^2}\right) - \frac{k_yT_e}{n_ee}\frac{k_\parallel^2\delta B_x\partial_x B_0}{m\mu_0(\omega^2 - c_s^2k_\parallel^2)} = -i\eta\frac{\delta B_x k_\perp^2}{\mu_0} \tag{A 5}$$

where $v_{de} = \frac{T_e}{n_eeB_0}\partial_x n_e$. One can now determine an expression for δu_x by rearranging Eq. A 2 to obtain:

$$\delta u_x = \frac{\omega k_x\left(\frac{\delta B_\parallel}{B_0}\right) + i\omega\frac{\delta B_\parallel}{B_0^2}\partial_x B_0 - \frac{k_\parallel\delta B_x}{\omega B_0}v_A^2(k_\perp^2 - i\frac{k_x}{B_0}\partial_x B_0)}{k_\perp^2 - \frac{1}{B_0^2}ik_x\partial_x B_0 - \frac{1}{B_0^2}\partial_x^2 B_0 + \frac{1}{B_0^3}\left(\partial_x B_0\right)^2} \tag{A 6}$$

If one now assumes pressure balance ($P + \frac{B_0^2}{2\mu_0} =$ constant) and negligible temperature gradients ($\partial_x T_e = 0$) the first and second derivatives from A 6 can be rewritten using the substitutions

$$\partial_x B_0 = -\frac{\mu_0 n_e e}{k_y}\omega^* \tag{A 7}$$

and

$$\partial_x^2 B_0 = \frac{\mu_0}{B_0}T_e\partial_x^2 n_e - \frac{\mu_0}{B_0}(\frac{\sqrt{\mu_0}n_e e}{k_y}\omega^*)^2 \tag{A 8}$$

Such that by now combining Eqs. A 6, A 7, A 8 and substituting into Eq. A 5 one can obtain the final dispersion relation

$$\underbrace{\left(\omega + \frac{k_\parallel\omega\frac{\delta B_\parallel}{\delta B_x}\left(k_x - i\frac{\mu_0 n_e e}{k_y}\omega^*\right) - \frac{k_\parallel^2}{\omega}v_A^2\left(k_\perp^2 - ie\frac{B_0}{v_A^2}\frac{k_x}{k_y}\omega^*\right)}{k_\perp^2 + i\frac{e}{v_A^2}\frac{k_x}{k_y}\omega^* - \frac{\mu_0}{B_0^3}T_e\partial_x^2 n_e}\right)}_{\text{Shear Alfvén Wave (a)}}\times$$

$$\underbrace{\left(1 - \frac{k_y\omega v_{de}}{(\omega^2 - c_s^2k_\parallel^2)}\right)}_{\text{Drift Wave (b)}} = \underbrace{-\frac{c_s^2k_\parallel^2\omega^*}{\omega^2 - c_s^2k_\parallel^2} - i\eta\frac{k_\perp^2}{\mu_0}}_{\text{Coupling Terms (c)}} \tag{A 9}$$

Eq. A 9 is similar to the dispersion relation found in Goldston's original derivation with two distinct branches, one for the shear Alfvén wave (a) and one for the Drift wave (b). However, by assuming non-zero values of β we introduce a new secondary coupling term (c) as well as modifying the second term in the shear Alfvén wave (a) part of the dispersion relation.

The derivation of this dispersion relation is not yet complete as the fluctuating quantities $\delta B_{\|}$ and δB_x are also functions of ω and $k_{\perp}$. In order to determine this relationship one can start with the MHD equation of motion linearized to first order,

$$(\delta \mathbf{J} \times \mathbf{B}) + (\mathbf{J} \times \delta \mathbf{B}) - \nabla \delta P_e = \rho_0 \partial_t \delta \mathbf{u}. \tag{A 10}$$

If one assumes that the zeroth order $\mathbf{J}$ arises from the zeroth order diamagnetic drift $u_d \approx \nabla P \times \mathbf{B}$ and the pressure profile $P(x)$ only varies in the x direction and the zeroth order $\mathbf{B}$ is $B_{\|}$ which points in the z direction, this means $\mathbf{J}$ only points in the y direction. The $\hat{x}$ component of Eq. A 10 can thus be written as:

$$\delta J_y B_0 - J_y \delta B_{\|} - \partial_x \delta P_e = -i\omega\rho_0 \delta u_x \tag{A 11}$$

Now using Ampere's law ($\nabla \times [\mathbf{B} + \delta\mathbf{B}] = \mu_0[\mathbf{J} + \delta\mathbf{J}]$) for both zeroth and first order one can rewrite Eq. A 11 and combine into Eq. A 6 to arrive at

$$\begin{aligned} &\frac{B_0}{\mu_0}(ik_{\|}\delta B_x - ik_x \delta B_{\|}) - \frac{\delta B_{\|}}{\mu_0}\partial_x B_{\|} - \partial_x \delta P_e = \\ &\qquad - i\omega\rho_0 \left(\frac{\omega k_x \left(\frac{\delta B_{\|}}{B_0}\right) + i\omega \frac{\delta B_{\|}}{B_0^2}\partial_x B_0 - \frac{k_{\|}\delta B_x}{\omega B_0} v_A^2 (k_{\perp}^2 - i\frac{k_x}{B_0}\partial_x B_0)}{k_{\perp}^2 - \frac{1}{B_0^2} ik_x \partial_x B_0 - \frac{1}{B_0^2}\partial_x^2 B_0 + \frac{1}{B_0^3}\left(\partial_x B_0\right)^2} \right) \end{aligned} \tag{A 12}$$

Now by expanding $\partial_x \delta P_e$ and combining with Eq. A 4, and Eq. A 6, one can group the δB_x and $\delta B_{\|}$ terms to arrive at the relation:

$$\frac{\delta B_{\|}}{\delta B_x} = \frac{\left(\begin{array}{c} \frac{ik_{\|}}{\mu_0} B_0 - \frac{i}{k_{\|} B_0}\partial_x T_e \partial_x n_e + \frac{k_x}{k_{\|} B_0} n_e \partial_x T_e \\ - \frac{\omega^2}{k_{\|} B_0 (\omega^2 - c_s^2 k_{\|}^2)}\partial_x n_e \left(k_x T_e + i\partial_x T_e\right) \\ + \frac{\omega}{(\omega^2 - c_s^2 k_{\|}^2)}\partial_x n_e \left(k_x T_e + i\partial_x T_e\right) \left(\frac{\frac{k_{\|}}{\omega B_0} v_A^2 (k_{\perp}^2 - i\frac{k_x}{B_0}\partial_x B_0)}{k_{\perp}^2 - \frac{1}{B_0^2} ik_x \partial_x B_0 - \frac{1}{B_0^2}\partial_x^2 B_0 + \frac{1}{B_0^3}(\partial_x B_0)^2} \right) \\ + \frac{\omega k_{\|}}{(\omega^2 - c_s^2 k_{\|}^2)} \frac{k_x T_e}{\omega m \mu_0}\partial_x B_0 + \frac{k_x T_e}{k_{\|} B_0}\partial_x n_e - i\frac{\omega k_{\|}}{(\omega^2 - c_s^2 k_{\|}^2)\omega m \mu_0}\partial_x T_e \partial_x B_0 \\ - i\frac{\partial_x T_e}{k_{\|} B_0}\partial_x n_e - i\omega\rho_0 \left(\frac{\frac{k_{\|}}{\omega B_0} v_A^2 (k_{\perp}^2 - i\frac{k_x}{B_0}\partial_x B_0)}{k_{\perp}^2 - \frac{1}{B_0^2} ik_x \partial_x B_0 - \frac{1}{B_0^2}\partial_x^2 B_0 + \frac{1}{B_0^3}(\partial_x B_0)^2} \right) \end{array} \right)}{\left(\begin{array}{c} \frac{ik_x}{\mu_0} B_0 + \frac{1}{\mu_0}\partial_x B_0 \\ + \frac{\omega}{(\omega^2 - c_s^2 k_{\|}^2)}\partial_x n_e \frac{(k_x T_e + i\partial_x T_e)}{\left(k_{\perp}^2 - \frac{1}{B_0^2} ik_x \partial_x B_0 - \frac{1}{B_0^2}\partial_x^2 B_0 + \frac{1}{B_0^3}(\partial_x B_0)^2\right)} \left(\frac{\omega k_x}{B_0} + \frac{i\omega}{B_0^2}\partial_x B_0\right) \\ - i\omega^2 \rho_0 \left(\frac{\left(\frac{k_x}{B_0}\right) + \frac{i}{B_0^2}\partial_x B_0}{k_{\perp}^2 - \frac{1}{B_0^2} ik_x \partial_x B_0 - \frac{1}{B_0^2}\partial_x^2 B_0 + \frac{1}{B_0^3}(\partial_x B_0)^2} \right) \end{array} \right)} \tag{A 13}$$

which can be substituted into Eq. A 9 to obtain a final dispersion relation explicitly in terms of ω and k.

Using the same assumptions a relation between δn_e and $\delta B_{\|}$ can be derived by taking Eq. A 12 to obtain:

$$\frac{B_0}{\mu_0}(ik_\parallel \delta B_x - ik_x \delta B_\parallel) - \frac{\delta B_\parallel}{\mu_0}\partial_x B_0 - \left(\frac{i}{k_\parallel}\frac{\delta B_x}{B_0}\partial_x T_e(\partial_x n_e + ik_x n_e) + \delta n_e(ik_x T_e + \partial_x T_e)\right) = -i\omega\rho_0\left(\frac{\omega k_x\left(\frac{\delta B_\parallel}{B_0}\right) + i\omega\frac{\delta B_\parallel}{B_0^2}\partial_x B_0 - \frac{k_\parallel \delta B_x}{\omega B_0}v_A^2(k_\perp^2 - i\frac{k_x}{B_0}\partial_x B_0)}{k_\perp^2 - \frac{1}{B_0^2}ik_x\partial_x B_0 - \frac{1}{B_0^2}\partial_x^2 B_0 + \frac{1}{B_0^3}\left(\partial_x B_0\right)^2}\right) \tag{A 14}$$

Choosing to ignore the RHS and expand out terms to group the $\delta B_\parallel$ and δn_e terms one then arrives at

$$\delta B_\parallel = -\delta n_e\left(\frac{ik_x T_e + \partial_x T_e}{\frac{B_0}{\mu_0}ik_x + \frac{1}{\mu_0}\partial_x B_0}\right) - \frac{\frac{i}{k_\parallel}\frac{\delta B_x}{B_0}\partial_x T_e(\partial_x n_e + ik_x n_e) - \frac{B_0}{\mu_0}ik_\parallel \delta B_x}{\frac{B_0}{\mu_0}ik_x + \frac{1}{\mu_0}\partial_x B_0} \tag{A 15}$$

Since the ratio more important than the additive offset, one can ignore the second term on the RHS and rearrange such that

$$\delta B_\parallel = \frac{-\delta n_e \mu_0 T_e}{B_0} \times \frac{ik_x + \frac{1}{T_e}\partial_x T_e}{ik_x + \frac{1}{B_0}\partial_x B_0} \tag{A 16}$$

and multiplying by the complex conjugate will yield

$$\delta B_\parallel = \frac{-\delta n_e \mu_0 T_e}{B_0} \times \frac{-k_x^2 - \frac{1}{T_e B_0}\partial_x T_e \partial_x B_0 - ik_x\frac{1}{B_0}\partial_x B_0 + ik_x\frac{1}{T_e}\partial_x T_e}{-k_x^2 - \left(\frac{1}{B_0}\partial_x B_0\right)^2} \tag{A 17}$$

Using the algebraic expressions for the gradients:

$$\begin{aligned} \partial_x \log(B_0) &= \frac{1}{B_0}\partial_x B_0 \\ \partial_x \log(T_e) &= \frac{1}{T_e}\partial_x T_e \end{aligned} \tag{A 18}$$

and substituting into Eq. A 17 yields

$$\delta B_\parallel = \frac{\delta n_e \mu_0 T_e}{B_0} \times \frac{-k_x^2 - \partial_x\log(B_0)\partial_x\log(T_e) - ik_x\partial_x\log(B_0) + ik_x\partial_x\log(T_e)}{k_x^2 + \left(\partial_x\log(B_0)\right)^2} \tag{A 19}$$

which can now be rearranged to yield the normalized fluctuation amplitude ratio in terms of β

$$\frac{\delta B_\parallel/B_0}{\delta n_e/n_e} = \frac{\beta}{2} \times \frac{-k_x^2 - \partial_x\log(B_0)\partial_x\log(T_e) - ik_x\partial_x\log(B_0) + ik_x\partial_x\log(T_e)}{k_x^2 + \left(\partial_x\log(B_0)\right)^2} \tag{A 20}$$

REFERENCES

Burke, AT, Maggs, JE & Morales, GJ 2000 Experimental study of fluctuations excited by a narrow temperature filament in a magnetized plasma. *Physics of Plasmas* **7** (5), 1397–1407.

Candy, J. 2005 Beta scaling of transport in microturbulence simulations. *Physics of Plasmas* **12** (7), 072307, arXiv: http://dx.doi.org/10.1063/1.1954123.

Carreras, B. A. 1997 Progress in anomalous transport research in toroidal magnetic confinement devices. *IEEE Transactions on Plasma Science* **25** (6), 1281–1321.

Carter, T. A. 2006 Intermittent turbulence and turbulent structures in a linear magnetized plasma. *Physics of Plasmas* **13** (1), 010701, arXiv: https://doi.org/10.1063/1.2158929.

Carter, T. A. & Maggs, J. E. 2009 Modifications of turbulence and turbulent transport associated with a bias-induced confinement transition in the large plasma device. *Physics of Plasmas* **16** (1), 012304.

Citrin, J, Garcia, J, Görler, T, Jenko, F, Mantica, P, Told, D, Bourdelle, C, Hatch, D R, Hogeweij, G M D, Johnson, T, Pueschel, M J & Schneider, M 2015 Electromagnetic stabilization of tokamak microturbulence in a high- β regime. *Plasma Physics and Controlled Fusion* **57** (1), 014032.

Doyle, E.J. 2007 Chapter 2: Plasma confinement and transport. *Nuclear Fusion* **47** (6), S18.

Everson, E. T., Pribyl, P., Constantin, C. G., Zylstra, A., Schaeffer, D., Kugland, N. L. & Niemann, C. 2009 Design, construction, and calibration of a three-axis, high-frequency magnetic probe (b-dot probe) as a diagnostic for exploding plasmas. *Review of Scientific Instruments* **80** (11), 113505.

Gekelman, W, Pribyl, P, Lucky, Z, Drandell, M, Leneman, D, Maggs, J, Vincena, S, Van Compernolle, B, Tripathi, SKP, Morales, G & others 2016 The upgraded large plasma device, a machine for studying frontier basic plasma physics. *Review of Scientific Instruments* **87** (2), 025105.

Goldston, Robert J & Rutherford, Paul Harding 1995 Introduction to plasma physics. CRC Press.

Horton, W., Correa, C., Chagelishvili, G. D., Avsarkisov, V. S., Lominadze, J. G., Perez, J. C., Kim, J.-H. & Carter, T. A. 2009 On generation of alfvénic-like fluctuations by drift wave–zonal flow system in large plasma device experiments. *Physics of Plasmas* **16** (9), 092102, arXiv: https://doi.org/10.1063/1.3211197.

Horton, W., Perez, Jean C., Carter, Troy & Bengtson, Roger 2005 Vorticity probes and the characterization of vortices in the kelvin-helmholtz instability in the large plasma device experiment. *Physics of Plasmas* **12** (2), 022303, arXiv: https://doi.org/10.1063/1.1830489.

Jenko, Frank & Scott, Bruce D 1999 Numerical computation of collisionless drift alfvén turbulence. *Physics of Plasmas* **6** (7), 2705–2713.

Kikuchi, M 1993 Prospects of a stationary tokamak reactor. *Plasma Physics and Controlled Fusion* **35** (SB), B39.

Lee, Wonjae, Angus, J.R., Umansky, Maxim V. & Krasheninnikov, Sergei I. 2015 Electromagnetic effects on plasma blob-filament transport. *Journal of Nuclear Materials* **463**, 765 – 768.

Liewer, Paulett C. 1985 Measurements of microturbulence in tokamaks and comparisons with theories of turbulence and anomalous transport. *Nuclear Fusion* **25** (5), 543.

Maggs, J. E., Carter, T. A. & Taylor, R. J. 2007 Transition from bohm to classical diffusion due to edge rotation of a cylindrical plasma. *Physics of Plasmas* **14** (5), 052507, arXiv: https://doi.org/10.1063/1.2722302.

Maggs, J E & Morales, G J 2012 Exponential power spectra, deterministic chaos and lorentzian pulses in plasma edge dynamics. *Plasma Physics and Controlled Fusion* **54** (12), 124041.

Morales, G J, Maggs, J E, Burke, A T & Peñano, J R 1999 Alfvénic turbulence associated with density and temperature filaments. *Plasma Physics and Controlled Fusion* **41** (3A), A519–A529.

Pace, D. C., Shi, M., Maggs, J. E., Morales, G. J. & Carter, T. A. 2008 Exponential frequency spectrum in magnetized plasmas. *Phys. Rev. Lett.* **101**, 085001.

Peñano, J. R., Morales, G. J. & Maggs, J. E. 2000 Drift-alfvÃ©n fluctuations associated with a narrow pressure striation. *Physics of Plasmas* **7** (1), 144–157, arXiv: https://doi.org/10.1063/1.873789.

Pueschel, MJ & Jenko, F 2010 Transport properties of finite-β microturbulence. *Physics of Plasmas* **17** (6), 062307.

Pueschel, MJ, Sydora, RD, Terry, PW, Tyburska-Pueschel, B, Francisquez, M, Jenko, F & Zhu, B 2020 Pair plasma instability in homogeneous magnetic guide fields. *Physics of Plasmas* **27** (10), 102111.

Pueschel, MJ, Terry, PW, Told, D & Jenko, F 2015 Enhanced magnetic reconnection in the presence of pressure gradients. *Physics of Plasmas* **22** (6), 062105.

Pueschel, M. J., Hatch, D. R., Görler, T., Nevins, W. M., Jenko, F., Terry, P. W. & Told, D. 2013 Properties of high-β microturbulence and the non-zonal transition. *Physics of Plasmas* **20** (10), 102301.

Pueschel, Moritz J, Jenko, F, Told, D & Büchner, J 2011 Gyrokinetic simulations of magnetic reconnection. *Physics of Plasmas* **18** (11), 112102.

Pueschel, Moritz J, Kammerer, M & Jenko, F 2008 Gyrokinetic turbulence simulations at high plasma beta. *Physics of Plasmas* **15** (10), 102310.

Pueschel, M J, Rossi, G, Told, D, Terry, P W, Jenko, F & Carter, T A 2017 A basic plasma test for gyrokinetics: GDC turbulence in LAPD. *Plasma Physics and Controlled Fusion* **59** (2), 024006.

Rechester, A. B. & Rosenbluth, M. N. 1978 Electron heat transport in a tokamak with destroyed magnetic surfaces. *Phys. Rev. Lett.* **40**, 38–41.

Rogers, Barrett N., Zhu, Ben & Francisquez, Manaure 2018 Gyrokinetic theory of slab universal modes and the non-existence of the gradient drift coupling (gdc) instability. *Physics of Plasmas* **25** (5), 052115, arXiv: https://doi.org/10.1063/1.5024748.

Schaffner, D. A., Carter, T. A., Rossi, G. D., Guice, D. S., Maggs, J. E., Vincena, S. & Friedman, B. 2013 Turbulence and transport suppression scaling with flow shear on the large plasma device. *Physics of Plasmas* **20** (5), 055907.

Smolyakov, A, Diamond, P & Kishimoto, Y 2002 Secondary instabilities of large scale flow and magnetic field in the electromagnetic short wavelength drift-alfven wave turbulence. *Physics of Plasmas* **9** (9), 3826–3834.

Snyder, P. B. & Hammett, G. W. 2001 Electromagnetic effects on plasma microturbulence and transport. *Physics of Plasmas* **8** (3), 744–749.

Terasawa, Toshio, Hoshino, Masahiro, Sakai, Jun-Ichi & Hada, Tohru 1986 Decay instability of finite-amplitude circularly polarized alfven waves: A numerical simulation of stimulated brillouin scattering. *Journal of Geophysical Research: Space Physics* **91** (A4), 4171–4187.

Terry, P.W., Carmody, D., Doerk, H., Guttenfelder, W., Hatch, D.R., Hegna, C.C., Ishizawa, A., Jenko, F., Nevins, W.M., Predebon, I., Pueschel, M.J., Sarff, J.S. & Whelan, G.G. 2015 Overview of gyrokinetic studies of finite- β microturbulence. *Nuclear Fusion* **55** (10), 104011.

Terry, P. W., Li, P.-Y., Pueschel, M. J. & Whelan, G. G. 2021 Threshold heat-flux reduction by near-resonant energy transfer. *Phys. Rev. Lett.* **126**, 025004.

Van Compernolle, B. & Morales, G. J. 2017 Avalanches driven by pressure gradients in a magnetized plasma. *Physics of Plasmas* **24** (11), 112302, arXiv: https://doi.org/10.1063/1.5001321.

Weidl, Martin S., Winske, Dan, Jenko, Frank & Niemann, Chris 2016 Hybrid simulations of a parallel collisionless shock in the large plasma device. *Physics of Plasmas* **23** (12), 122102, arXiv: https://doi.org/10.1063/1.4971231.

Weiland, J. & Hirose, A. 1992 Electromagnetic and kinetic effects on the ion temperature gradient mode. *Nuclear Fusion* **32** (1), 151.

Whelan, G. G., Pueschel, M. J. & Terry, P. W. 2018 Nonlinear electromagnetic stabilization of plasma microturbulence. *Phys. Rev. Lett.* **120**, 175002.

Zhou, S., Heidbrink, W. W., Boehmer, H., McWilliams, R., Carter, T. A., Vincena, S., Friedman, B. & Schaffner, D. 2012 Sheared-flow induced confinement transition in a linear magnetized plasma. *Physics of Plasmas* **19** (1), 012116, arXiv: https://doi.org/10.1063/1.3677361.

Zimbardo, G., Perri, S., Pommois, P. & Veltri, P. 2012 Anomalous particle transport in the heliosphere. *Advances in Space Research* **49** (11), 1633 – 1642, advances in theory and observation of solar system dynamics - I.